Langmuir

Article

pubs.acs.org/Langmuir

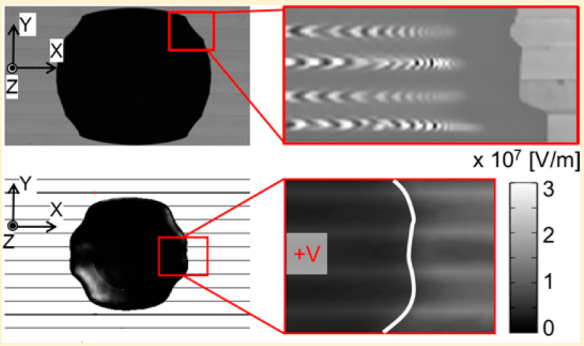
Experimental and Numerical Insights into Isotropic Spreading and Deterministic Dewetting of Dielectrowetted Films

A. C. Russell,[†] W. L. Hsieh,[‡] K. C. Chen,[‡] and J. Heikenfeld*[,†]

[†]Novel Device Laboratory, School of Electrical Engineering and Computing Systems, University of Cincinnati, Cincinnati, Ohio 45221, United States

[‡]Institute of Applied Mechanics, National Taiwan University, Taipei 106, Taiwan

ABSTRACT: Dielectrowetting effects of surface wrinkling, isotropic vs anisotropic spreading, electrode geometry, and deterministic dewetting are presented both experimentally and by 3D numerical modeling. The numerical results are generated by COMSOL in conjunction with the phase-field and electrohydrodynamic methods, including comparisons to experimental data. The dynamic behavior of the two-phase system has been accurately characterized on both the macro- and microscopic level. This work provides a deeper theoretical insight into the operating physics of dielectrowetting superspreading devices.



INTRODUCTION

Nonuniform electric fields can be used to move dielectric particles or fluids in a controlled manner,[1−4] and with adequately high alternating frequencies even semi-insulating fluids can be manipulated. This approach is classically known as dielectrophoresis (DEP)[5−10] and more recently has been implemented for superspreading of dielectric fluids such as dielectrowetting (DEW),[6,9,10] including applications such as optical shutters.[11,12] DEW devices typically consist of evenly spaced interdigitated conducting electrodes, and much work has been done to explain the DEP phenomenon on interdigitated electrodes.[5,13−18] However, to our knowledge, no in-depth 3D modeling has been reported for DEW devices, nor has theory or specific experiment for the factors limiting isotropic superspreading been presented. Previous theoretical or modeling work of interdigitated electrodes includes use of series expansion of Green's function[18] and the Fourier series.[16,17] Unfortunately, all are approximations at best, and many do not provide insight into the deeper physics of operation specific to DEW devices. Furthermore, point charge, charge density, finite difference, and integration have all been used successfully to characterize the E-field for DEP devices,[19−21] yet the same approach has yet to be applied to DEW devices.

In this work, we present both experimental and modeling insights into the anisotropic nature of fluid superspreading, effects of electrode geometry, and surface wrinkling of the DEW superspread films.[10] Modeling comprises 3D simulations meshed with free triangle, third-order polynomial solutions. Results are presented for DEW analysis using both the phase-field method[22] and electrohydrodynamic method.[23] These modeling results also confirm our previous understanding of deterministic fluid splitting.[24−26] This work provides a basis for both deeper theoretical insight into the physics of DEW devices and confirms that 3D modeling is a powerful and predictive tool for DEW devices.

BASIS FOR 3D NUMERICAL MODELING

Phase-Field Method (PFM) for DEW Devices. The PFM was used to numerically solve the droplet movement during dielectrowetting and dewetting, tracing the dynamic topological changes of the ink−air interface.[22] PFM characterizes this boundary using the ink's free energy while incorporating the interaction of fluids and microstructured surfaces. A side view of the parallel 40 μm interdigitated DEW device in the off state is seen in Figure 1a. In the on-state as shown in Figure 1b, the diffusive transition region of the ink/air is modeled using a thin layer that smoothly connects one region to the other using a continuous phase-field variable, ϕ, which varies from −1 for ink to +1 for air. The utilized volumetric fractions were $\overline{V}_{ink} = (1 - \phi)/2$ and $\overline{V}_{air} = (1 + \phi)/2$. Therefore, the physical properties can then be described across the interface in terms of ϕ as follows:

$$\rho = \rho_{ink}\overline{V}_{ink} + \rho_{air}\overline{V}_{air}$$
$$\mu = \mu_{ink}\overline{V}_{ink} + \mu_{air}\overline{V}_{air}$$
$$\varepsilon = \varepsilon_{ink}\overline{V}_{ink} + \varepsilon_{air}\overline{V}_{air} \quad (1)$$

where ρ, μ, and ε represent the density, viscosity, and relative dielectric constant of fluids. In the diffusive-interface picture,

Received: October 14, 2014
Revised: December 1, 2014
Published: December 8, 2014

ACS Publications © 2014 American Chemical Society

DOI: 10.1021/la504066j
Langmuir 2015, 31, 637−642

FROM LANGMUIR

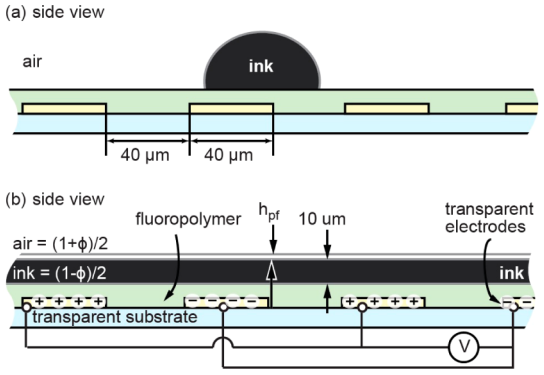


Figure 1. (a) Diagram side view of a DEW optical shutter in the (a) off state (optical transmission) and (b) on state (no optical transmission).

the transition between ink and air follows the Cahn–Hilliard convection equation:[27]

$$\frac{\partial \varphi}{\partial t} + \mathbf{u}\cdot\nabla(\varphi) = \nabla\cdot(M\nabla G) \tag{2}$$

where $\mathbf{u}$ represents the fluid velocity, M denotes the mobility (or diffusion coefficient), and G is the chemical potential. Mobility can be expressed as $M = \chi h_{PF}^2$, where χ is the characteristic mobility and h_{PF} is the capillary width that scales with the thickness at the diffusion interface in PFM (Figure 1). The chemical potential G, which is a partial differential of the total free energy with respect to ϕ, is expressed as $G = \lambda[-\nabla^2\phi + \phi(\phi^2 - 1)/h_{PF}^2]$, where λ is the energy density parameter. In addition, λ and h_{PF} are related to the interfacial tension as $\gamma = 2\sqrt{2}\lambda/h_{PF}$.

Boundary Conditions for PFM. In the formulation of PFM, the fluoropolymer surface is considered as a wetted wall, where we can specify a wetted contact angle θ_w related to ϕ for the fluids in the form

$$\mathbf{n}\cdot\nabla\varphi = \cos\theta_w|\nabla\varphi| \tag{3}$$

where $\mathbf{n}$ is the unit vector normal to the wall.

Electrohydrodynamic Method (EHD) for DEW Devices. The movement of the immiscible two-phase flow and transport of mass and momentum are governed by the incompressible Navier–Stokes equations:[23]

$$\rho\left(\frac{\partial \mathbf{u}}{\partial t} + \mathbf{u}\cdot\nabla\mathbf{u}\right) = -\nabla p + \nabla\cdot\mu(\nabla\mathbf{u} + \nabla\mathbf{u}^{\mathrm{T}}) + F_s + F_D \tag{4}$$

$$\nabla\cdot\mathbf{u} = 0 \tag{5}$$

where ρ and μ are the density and viscosity of the fluids expressed in terms of ϕ as expressed in eq 1, and p is the pressure in the fluid. Volumetric surface tension, F_s, is calculated via $F_s = G\nabla\phi$ and is approximately zero except at the diffusive ink–air interface. F_D is the DEP force based on the dielectrophoretic force[7,11,12,28]

$$F_D = \frac{1}{2}\varepsilon_0(\varepsilon - 1)\nabla E^2 \tag{6}$$

where ε_0 is the vacuum permittivity, ε is the dielectric constant of fluids in terms of ϕ as expressed in eq 1, and E is the electric field. The ink, air, and fluoropolymer are considered to be dielectric materials; therefore, the free electric charges can be neglected in the DEW simulation. Hence, in the electrostatic field formulation, the electric field is governed by the following Laplace equation:

$$\nabla\cdot(\varepsilon_0\varepsilon_r E) = 0 \tag{7}$$

where ε_r is the relative permittivity of the numerical domains for both solid dielectrics and fluids. Once the electric field is determined, the effect of the DEP force F_D acting on the ink could be realized according to the Navier–Stokes equation in eq 4.

Boundary Conditions for EHD. When solving the momentum conservation equation, the no-slip boundary condition (i.e., $\boldsymbol{\mu} = 0$) is utilized at the fluoropolymer surface, and the rest of the boundaries are set to equal to 1 atm (ambient pressure). When solving the electrostatic field, the zero charge condition (i.e., $\mathbf{n}\cdot\mathbf{D} = 0$) is adopted at the boundaries with exception of the patterned electrode parts. Dc voltage was used in the simulations; therefore, the electric field could be calculated using $E = -\nabla V$.

RESULTS

The geometries and dielectric layers used for testing and simulation vary; therefore, any pertinent details for each test will be addressed in the subsections individually. However, in all situations, the fabrication of the indium–tin oxide (ITO) electrodes on glass substrates, subsequent dielectric coating, and use of liquid crystal fluid are all similar to our previous work.[11,12] We present and discuss the results of this present work in five subsections. First, surface wrinkling is numerically and experimentally verified. Second, we discuss the droplet spreading anisotropy and effect of droplet size on this anisotropy. Third, the impact of the dielectric thickness on spreading behavior is analyzed. Fourth, electrode morphology and droplet wetting behavior are discussed. Lastly, agreement is demonstrated for both experiment and modeling for the dynamic process of fluid splitting and dewetting.

Surface Wrinkling. Parallel 40 μm interdigitated electrodes coated in ~50 nm of fluoropolymer (Cytonix Fluoropel 1601V) were used for the experimental results seen in Figure 2a and simulations in Figure 2b–d. The experimental wrinkling photographs in (a) were taken using both a conventional optical microscope (left) and interferometric optical microscope (right). Similar surface wrinkling is also observed for the modeled results. The nonuniform electric field between the parallel electrodes is numerically shown in Figure 2b. It can be found that the electric strength at the edge of the electrodes is relatively high due to the fringe effect, thus leading to a strong gradient of electric field. This result indicates that the ink droplet experiences a relatively high dielectrophoretic force at the electrodes edge, resulting in a periodic deformation at the ink surface.[13,29,30] Here, to clearly show the distribution of electrical potential, we used a 4 μm dielectric layer with 300 V_P in the simulation as shown in the close-up view of Figure 2c. Here, $\pm V = \pm 300$ V_P. In addition, a contour plot of the magnitude of the dielectrophoretic force based on eq 6 is shown in Figure 2d. The dense contour lines near the electrode edges indicate that the strongest force is in these regions, hence causing the observed surface wrinkling. This conclusion is consistent with periodic deformation observed at a dielectric liquid surface in similar devices.[13,29]

Insights into Anisotropic Spreading. During device testing, both isotropic and highly anisotropic spreading were both previously observed, and before this work, it was not understood what factors promote isotropic spreading. Using

REPRINTED FROM LANGMUIR

DOI: 10.1021/la504066j
Langmuir 2015, 31, 637–642

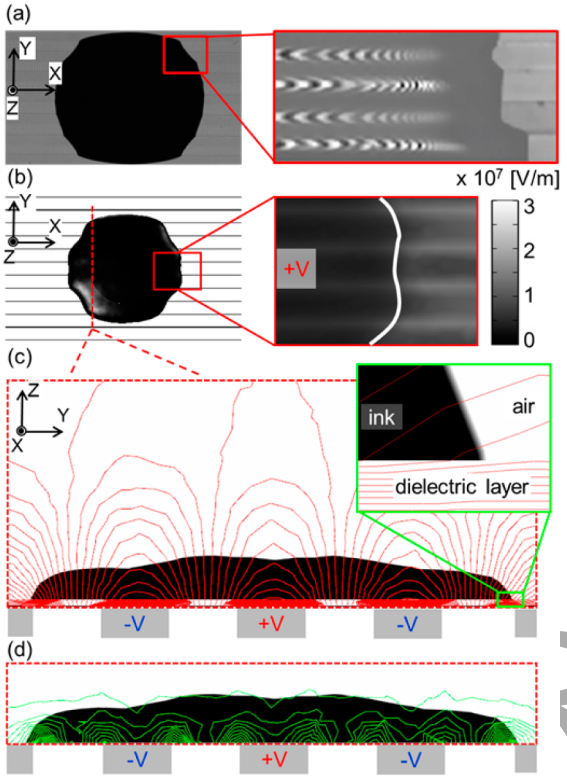


Figure 2. (a) Top view photograph (left) of droplet transitioning from a dewetted droplet to the wetted film state on parallel electrodes. The surface wrinkling is also seen in the magnified optical interferometer image (right). (b) Numerical results as viewed from (left) above as ink spreads and (right) a close-up of numerically observed surface wrinkling where the slice is taken at the liquid contact line. (c) Side view of numerical simulated electric potential field lines. (d) Side view of numerical simulated magnitude of the dielectrophoretic force.

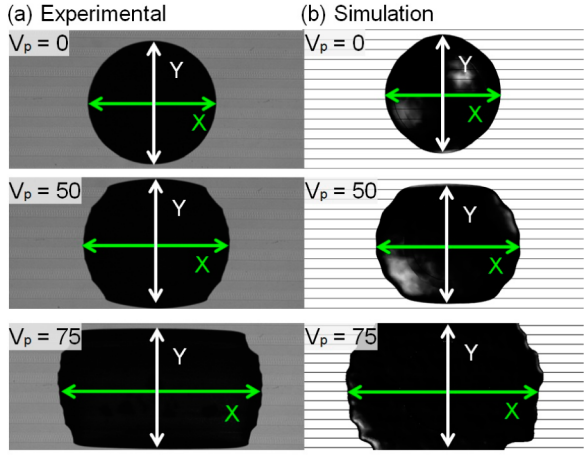


Figure 3. (a) Top view of the liquid crystal droplet placed on dielectrowetting device and the spreading resulting from 0, 50, and 75 V_p. Notice the greater spread in the *X* direction versus *Y* for all applied voltages. (b) Simulation results of 0, 50, and 75 V_p show the same behavior.

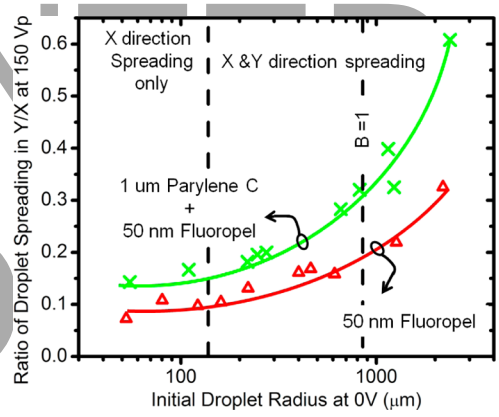


Figure 4. As droplet radius increases, the spreading becomes more isotropic on thin and thick dielectrics.

devices with parallel 40 μm interdigitated electrodes with splitting features coated in 1 μm Parylene C + ~50 nm Fluoropel,[12] it was observed that as the liquid crystal droplet diameter decreases, isotropic spreading across electrodes as seen by Zhao et al.[11] would not occur.

In order to understand a droplet size dependence on anisotropic spreading, gravitational effects and Laplace pressure are further considered. When using a single plate design (open air), the ratio of gravity to surface tension force is characterized by the Bond number,[31] defined as $(\rho g d^2)/\gamma_{LV}$ where $\rho \sim 1100$ kg m^{-3} (droplet density), g is the acceleration due to gravity, $\gamma_{LV} \sim 39$ mN m^{-1}, and d is droplet diameter. Additionally, the Laplace Pressure defined as $P_L = \gamma(1/R_H + 1/R_V)$ is also clearly dependent on droplet size (radii R). Therefore, both detailed experiment and modeling were performed to investigate the effect of droplet size on isotropic spreading.

For both experiment and modeling, parallel 40 μm interdigitated electrodes coated in ~50 nm of fluoropolymer displayed anisotropic spreading with different applied voltages as seen in Figure 3.[30] When the device is actuated at 75 V_p, the nonuniform spreading motion along the *X* direction is visually obvious experimentally (Figure 3a) and numerically (Figure 3b). Next, tests of various droplet sizes (radius at 0 V_p) and spreading behavior were then performed on parallel 40 μm interdigitated electrodes coated in ~50 nm Fluoropel (thin) as well as 1 μm Parylene C + ~50 nm Fluoropel (thick) devices. Looking to Figure 4, the ratio between the spreading in the *X* versus *Y* direction using different initial droplet sizes and 150 V_p is seen using both the thin vs thick dielectric coatings.

When the droplet radius is below ~150 μm, the spreading is highly anisotropic (Figure 4, left). As the droplet volume increases, the droplet spreading becomes more uniform (Figure 4, middle). When the droplet radius is >950 μm, we speculate that the effects of gravity and weaker Laplace pressure allow more isotropic spreading (Figure 4, right).[32] The Bond number reaches unity at a diameter of 1900 μm. At this point, we conclude that isotropic spreading can be achieved by using droplets with radii greater than approximately 1 mm in the dewetted state. As shown in our previous work, the droplet radii can simply be determined by adding splitting features with the appropriate pitch in between them.[11,12]

Effect of Dielectric Thickness. The effect of the dielectric thickness on isotropic vs anisotropic spreading for a fixed volume droplet was also explored (Figure 5a). Various voltages on parallel 40 μm interdigitated electrodes coated in ~50 nm Fluoropel as well as 1 μm Parylene C + ~50 nm Fluoropel were investigated with a droplet of volume ~5 nL applied in all tests (radius = 140 μm). Referring to Figure 2c, it is obvious that the field lines are more concentrated near the substrate. The use of a thicker or thinner dielectric does not seem to result in significantly more uniform spreading, as seen in Figure 5a. This

PRINTED ERROR LANGMUIR

DOI: 10.1021/la504066j
Langmuir 2015, 31, 637−642

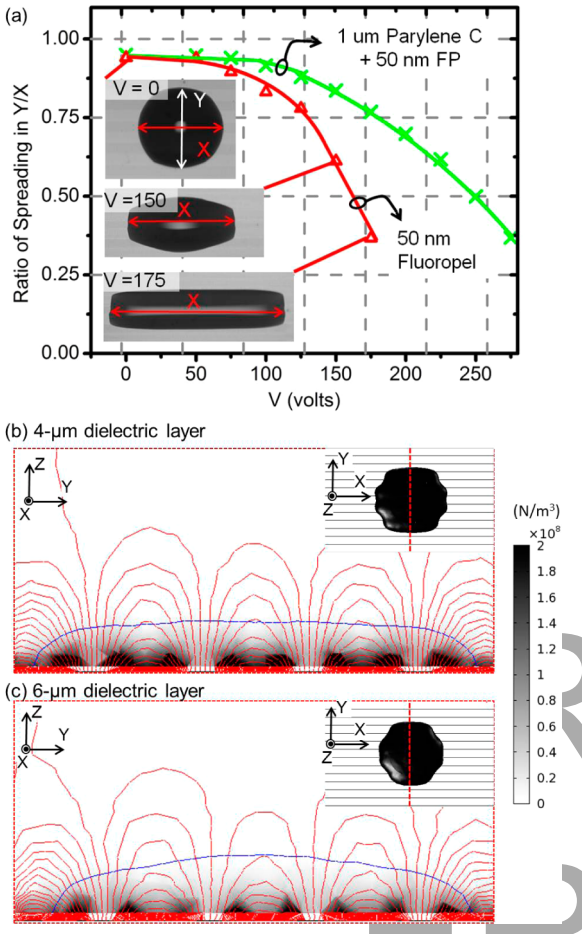


Figure 5. Spreading of a single droplet over thin vs thick dielectrics (a) experimentally and (b, c) numerically both show that dielectric thickness does not strongly effect isotropic superspreading. In (b, c), the grayscale distribution denotes the magnitude of dielectrophoretic force.

is further supported in Figure 5b,c, which provides a side view cut in the center of the droplet of numerical simulated electric potential field lines for a 4 and 6 μm dielectric layer with 300 V_p.

Dielectric thickness only affects the voltage required for a given amount of spreading, which is expected since the divergence of the E-field decreases with distance from the electrodes and a thicker dielectric causes the fluid to be further away from the electrodes. Of course, very thick dielectrics could at some thickness reach the point where superspreading cannot be achieved at all, as the field strengths at the dielectric surface would be very weak.

Effect of Electrode Morphology. Electrode geometry was explored as all previous DEW work used parallel electrodes only. Less homogeneous electrode geometries were explored to see if they could promote more isotropic spreading using an interdigitated sawtooth and zipper-style pattern using a ~50 nm Fluoropel dielectric. The sawtooth pattern exhibited very poor or no spreading and is not presented here in detail. Therefore, the focus here is on the zipper pattern experimental data shown in Figure 6. The zipper pattern has E-fields which are diverging in both the *x*,*z* and *y*,*z* planes of the substrate surface (*z*-axis being the surface normal), unlike parallel electrodes where the divergence is in limited in the direction of only *x*,*z* or *y*,*z*. The zipper-style pattern still requires a long address line electrode to

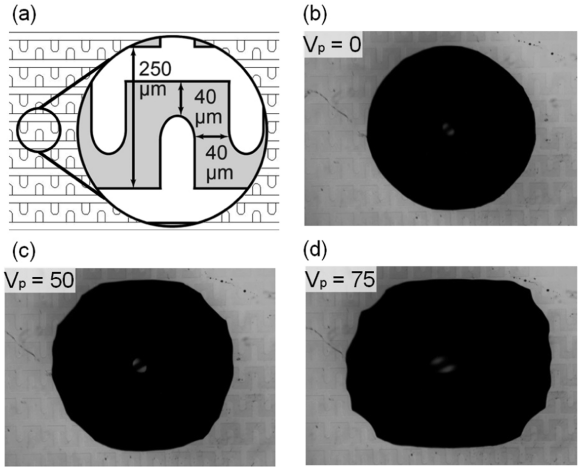


Figure 6. (a) Diagram and (b–d) optical microscope top view of the spreading liquid crystal droplet at (b) $V_p = 0$, (c) $V_p = 50$, and (d) $V_p = 75$ with zipper patterned electrodes (the ITO is light, the glass is dark). Isotropic spreading was not achieved but rather limited by the long, parallel electrodes.

bring in voltage from the edges of the substrate, and over the middle of address line electrode the E-field divergence is weaker than it would be at electrode edges. This was also confirmed in the results of Figure 2d. This is clearly visible as the droplet wets against the continuous portion of the address line but does not wet further beyond that. We therefore speculate that if superspreading is to be improved in terms of its isotropicity, then both *x*,*z* and *y*,*z* field divergences between electrode edges are needed, and it must be achieved without long electrode lines which have weaker field divergence over their middle surface. This could be achieved potentially by very narrow address lines (using higher conductivity and higher resolution patterning) or through voltage connections through underlying via layers and a checkerboard or honeycomb pattern of spaced electrodes. Fabrication of such structures is complex and beyond the scope of this work. Therefore, using the current toolset of materials and electrodes available in this work, the only means to achieve isotropic spreading we have seen to be viable is by using larger droplet sizes.

Predictive Splitting Process. The 3D numerical modeling is also able to simulate the dewetting when using splitting features to deterministically cause the dewetting.[11,12] Here, the regular splitting features are built into the simulation domain with the same parameters as experimental devices shown in Figure 7a. The side-wall angle of the splitting features is 50°, simulating the dewetting features characterized in detail by Russell et al.[12] In addition, the pitch sizes adopted here are 850, 1300, and 2000 μm. The trend in reduction of dewetting time by scaling down the splitting feature pitch is both experimentally (Figure 7b) and numerically shown in Figure 7c. The diagram of the top view of the splitting process with pitch ~1300 μm is shown in the inset of Figure 7c, from which it can be found that the splitting process nucleates at the splitting features. Close correspondence can be seen when comparing the results of dewetting in Figure 7 experimentally (b) and numerically (c). The numerical model also accurately follows the trend in dewetting speed, but the numerical results are less affected by the change in splitting feature pitch. The reason for this discrepancy is not understood at this time.

PRINTED FROM LANGMUIR

DOI: 10.1021/la504066j
Langmuir 2015, 31, 637–642

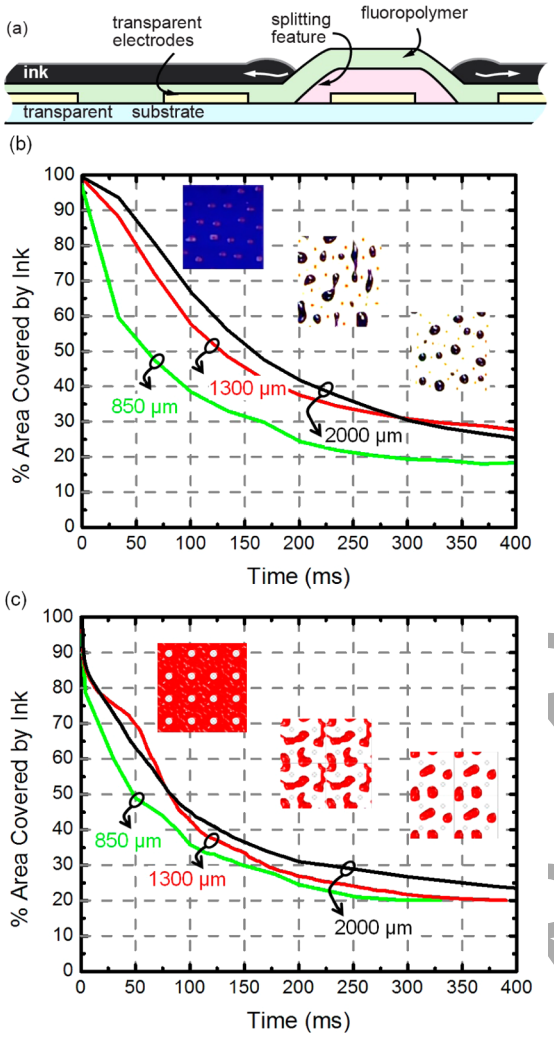


Figure 7. (a) Diagram of DEW optical shutter, side view. Splitting speeds of various splitting feature pitches ranging from 850 to 2000 μm obtained from (b) experiments and (c) simulations. Inset: schematic of top view of the splitting process with the pitch width 1300 μm.

SUMMARY AND CONCLUSION

This work has provided deeper microfluidic insight into the dielectrowetting superspreading devices via additional experimentation coupled with numerical simulations. Using the PFM and EHD model, the dynamic behavior of the two-phase system has been accurately characterized on both the macro- and microscopic level. The effects of surface wrinkling, anisotropic spreading, and inhomogeneous fields have been experimentally explored, modeled, and presented here. Isotropic spreading has been shown to be limited, at least with the current materials and geometries used herein, to occur only for larger droplet sizes where it is speculated that gravity and weaker Laplace pressure facilitate the spreading. These results of this work can be used to further optimize dielectrowetting superspreading devices for various applications. The modeling work may also allow researchers to more rapidly investigate alternate designs beyond those currently reported.

AUTHOR INFORMATION

Corresponding Author

*E-mail heikenjc@ucmail.uc.edu (J.H.).

Author Contributions

A.C.R. and W.L.H. contributed equally to this work and should both be considered first authors.

Notes

The authors declare no competing financial interest.

ACKNOWLEDGMENTS

The authors gratefully acknowledge partial support from the National Science Foundation (ECCS 1001146, ECCS 1231668), from Sun Chemical Corp, and from National Science Council (NSC 103-2917-I-002-162). The authors thank Dr. Russ Schwartz (Sun Chemical Corp.) and Mr. Fujino Nobutaka (DIC Corp., Japan) for providing fluid materials. The authors also thank Prof. Glen McHale (Northumbria University) and Prof. Carl Brown (Nottingham Trent University) for early input and guidance on dielectrowetting superspreading operation.

REFERENCES

(1) Pellat, H. Mesure de la force agissant sur les diélectriques liquides non électrisés placés dans un champ élitrique. *C. R. Acad. Sci. Paris* **1895**, *119*, 691−694.

(2) Pohl, H. A.; Pohl, H. *Dielectrophoresis: The Behavior of Neutral Matter in Nonuniform Electric Fields*; Cambridge University Press: Cambridge, 1978.

(3) Pohl, H. A. Some effects of nonuniform fields on dielectrics. *J. Appl. Phys.* **2004**, *29* (8), 1182−1188.

(4) Bruus, H. *Theoretical Microfluidics*; Oxford University Press: New York, 2008; Vol. *18*.

(5) Green, N. G.; Ramos, A.; Morgan, H. Numerical solution of the dielectrophoretic and travelling wave forces for interdigitated electrode arrays using the finite element method. *J. Electrost.* **2002**, *56* (2), 235−254.

(6) McHale, G.; et al. Dielectrowetting driven spreading of droplets. *Phys. Rev. Lett.* **2011**, *107* (18), 186101.

(7) Cheng, C.-C.; Chang, C. A.; Yeh, J. A. Variable focus dielectric liquid droplet lens. *Opt. Express* **2006**, *14* (9), 4101−4106.

(8) Ren, H.; et al. Voltage-expandable liquid crystal surface. *Lab Chip* **2011**, *11* (20), 3426−3430.

(9) McHale, G.; et al. Developing interface localized liquid dielectrophoresis for optical applications. *Photonics Asia* **2012**, 855703−855703-8.

(10) McHale, G.; et al. Voltage-induced spreading and superspreading of liquids. *Nat. Commun.* **2013**, *4*, 1605.

(11) Zhao, R.; et al. Large area and low power dielectrowetting optical shutter with local deterministic fluid film breakup. *Appl. Phys. Lett.* **2013**, *103* (22), 223510.

(12) Russell, A. C.; et al. Scaling dielectrowetting optical shutters to higher resolution: microfluidic and optical implications. *Langmuir* **2014**, *30*, 5357.

(13) Brown.; et al. Analysis of a static undulation on the surface of a thin dielectric liquid layer formed by dielectrophoresis forces. *J. Appl. Phys.* **2011**, *110* (2), 024107.

(14) Jackson, J. D. *Classical Electrodynamics*, 3rd ed.; Wiley-VCH: Weinheim, 1998; Vol. *1*, p 832.

(15) Lorrain, P.; Corson, D. *Electromagnetic Fields and Waves*; W.H. Freeman & Co. Ltd.: New York, 1970.

(16) Masuda, S.; Washizu, M.; Iwadare, M. Separation of small particles suspended in liquid by nonuniform traveling field. Industry Applications. *IEEE Trans.* **1987**, No. 3, 474−480.

(17) Morgan, H.; et al. The dielectrophoretic and travelling wave forces generated by interdigitated electrode arrays: analytical solution using Fourier series. *J. Phys. D: Appl. Phys.* **2001**, *34* (10), 1553.

PRINTED FROM LANGMUIR

DOI: 10.1021/la504066j
Langmuir 2015, 31, 637−642

(18) Wang, X.; et al. A theoretical method of electrical field analysis for dielectrophoretic electrode arrays using Green's theorem. *J. Phys. D: Appl. Phys.* **1996**, *29* (6), 1649.
(19) Rosenthal, A.; Voldman, J. Dielectrophoretic traps for single-particle patterning. *Biophys. J.* **2005**, *88* (3), 2193−2205.
(20) Wang, X.-B.; et al. Selective dielectrophoretic confinement of bioparticles in potential energy wells. *J. Phys. D: Appl. Phys.* **1993**, *26* (8), 1278.
(21) Hughes, M. P.; et al. Dielectrophoretic forces on particles in travelling electric fields. *J. Phys. D: Appl. Phys.* **1996**, *29* (2), 474.
(22) Yue, P.; et al. A diffuse-interface method for simulating two-phase flows of complex fluids. *J. Fluid Mech.* **2004**, *515*, 293−317.
(23) Castellanos, A.; et al. Electrohydrodynamics and dielectrophoresis in microsystems: scaling laws. *J. Phys. D: Appl. Phys.* **2003**, *36* (20), 2584.
(24) Redon, C.; et al. Dynamics of dewetting. *Phys. Rev. Lett.* **1991**, *66* (6), 715.
(25) Taylor, G.; Michael, D. On making holes in a sheet of fluid. *J. Fluid Mech.* **1973**, *58* (04), 625−639.
(26) Sharma, A.; Ruckenstein, E. Dewetting of solids by the formation of holes in macroscopic liquid films. *J. Colloid Interface Sci.* **1989**, *133* (2), 358−368.
(27) Cahn, J. W.; Hilliard, J. E. Free energy of a nonuniform system. I. Interfacial free energy. *J. Chem. Phys.* **2004**, *28* (2), 258−267.
(28) Wells, G.; et al. Fast reconfigurable liquid optical interface: investigation of higher harmonics in the periodic liquid surface wrinkle. *SPIE Photonics Eur.* **2010**, 77160G-77160G-7.
(29) Brown, C.; et al. Voltage-programmable liquid optical interface. *Nat. Photonics* **2009**, *3* (7), 403−405.
(30) Brown, C.; et al. Amplitude scaling of a static wrinkle at an oil-air interface created by dielectrophoresis forces. *Appl. Phys. Lett.* **2010**, *97* (24), 242904.
(31) Cooney, C. G.; et al. Electrowetting droplet microfluidics on a single planar surface. *Microfluid. Nanofluid.* **2006**, *2* (5), 435−446.
(32) Mugele, F.; Baret, J.-C. Electrowetting: from basics to applications. *J. Phys.: Condens. Matter* **2005**, *17* (28), R705.

REPRINTED FROM LANGMUIR

DOI: 10.1021/la504066j
Langmuir 2015, 31, 637−642